Self-Supported Ultra-Active NiO-Based Electrocatalysts for Oxygen Evolution Reaction by Solution Combustion.

Alberto Bucci,[a,*] Miguel García-Tecedor,[b,e] Sacha Corby,[c] Reshma Rao,[c] Vlad Martin-Diaconescu,[d] Freddy E. Oropeza,[e] Víctor A. de la Peña O'Shea,[e] James R. Durrant,[c,f,] Sixto Giménez,[b,*] Julio Lloret-Fillol[a,g,*]

[a] Institute of Chemical Research of Catalonia (ICIQ), The Barcelona Institute of Science and Technology, Avinguda Països Catalans 16, 43007 Tarragona, Spain.

[b] Insitute of Advanced Materials (INAM), University Jaume I, 12071 Castello de la Plana, Spain

[c] Department of Chemistry and Centre for Plastic Electronics, Imperial College London, London W12 0BZ, U.K.

[d] CELLS−ALBA Synchrotron E-08290 Cerdanyola del Vallès, Barcelona, Spain

[e] Madrid Photoactivated Processes Unit, IMDEA Energy Institute, Av. Rámon de la Sagra, 3 Parque Tecnologico de Mostoles, 28935, Mostoles, Madrid, Spain

[f] SPECIFIC, College of Engineering, Swansea University, Bay Campus, Fabian Way, Swansea SA1 8EN, U.K.

[g] Catalan Institution for Research and Advanced Studies (ICREA), Passeig Lluïs Companys, 23, 08010, Barcelona (Spain).

* corresponding authors: e-mail: abucci@iciq.es (AB); sjulia@fca.uji.es (SG); jlloret@iciq.es (JL-F)

Abstract.

Oxygen evolution reaction (OER) is a fundamental process to develop a technology that can drive the energy transition towards renewable and sustainable fuels. Nevertheless, efficient and straightforward methodologies to obtain outperforming and stable electrodes need to be implemented to approach this technology to real applications. Recently, self-supported catalysis emerged as a promising solution. However, catalyst design is still limited by the low chemical tunability and elevated preparation time and costs. Herein, a solution combustion (SC) methodology is described to produce designed self-supported electrocatalysts that excel in OER and mitigate previous limitations. M-doped NiO-based electrocatalysts (with M = Fe, Co, Mn, and Zn) were self-supported by the SC method on nickel foam, and demonstrate to overperform analogous benchmarked catalysts prepared by other methods. Notably, in Fe-doped NiO, the overpotential required to drive OER at 10 mA/cm^2 was found to be 190 mV, the lowest reported so far for metal oxides electrocatalysts at pH 13. By the combination of spectroelectrochemical (SEC) and electrochemical impedance spectroscopy (EIS), we studied the role of the metal dopant cation, showing that dopant metals assist the formation of the active species responsible for the high (electro)catalytic activity. We envision that the presented simple, cost-time efficient methodology would stimulate the preparation and study of effective self-supported metal-oxide catalysts for a broad range of applications.

Introduction. The adaptation of our fossil fuel-based society to one pivoted on renewable energy sources is a major issue of our civilization to achieve a more sustainable future.[1, 2] However, this transition requires the development of catalysts that can promote the transformation of abundant raw materials in fuels of easy storing and fine chemicals.[3-8] To this end, the oxidation of water to oxygen, i.e., the oxygen evolution reaction (OER), is arguably essential to obtain solar fuels such as hydrogen (*via* water reduction) or carbon products (*via* CO_2 reduction).

Over the last decades, much effort has been devoted to lower the required overpotential for the oxygen evolution reaction and increase the durability of OER catalysts. Nevertheless, the requirements needed for industrial applications are very demanding in terms of both corrosive reaction environments and the high current densities.[9] Self-supported catalysis recently emerged to overcome such limitations, allowing to improve the catalytic activity, the stability, and the catalyst loading at the same time.[10, 11] The success of this strategy consists in the elimination of the binder, which often obstructs the active sites, limits reagents/products diffusion and impedes a good electric connexion with the current collector.[10]

The most used methods to prepare self-supported catalysts include thermal decomposition methods,[12-14] hydro/solvothermal synthesis,[15-17] electrodeposition,[18-20] corrosion chemistry,[21] and chemical vapor deposition[22, 23] that has been largely adopted to prepare many catalytically active phases as metal oxides,[12-14] metal (oxy)hydroxides[18, 21, 24-27] and metal phosphates.[27-29]

Although many steps forward have been made, progress is slowed by limitations in the rational design of such catalysts, for which the number and nature of the active sites are often unknown or poorly defined. The problem is defined at two different levels; from a fundamental perspective, there is a clear need to develop novel synthetic methodologies

that bring together the rational design (chemical tunability), the high applicability (performance and stability), and improved understanding at atomic level (*in situ* analyses). Instead, from the application perspective, the full catalyst development also needs to account for other factors as time-efficiency, cost-effectiveness, and scalability. To address both points, we resorted to solution combustion (SC) synthesis. Despite this is a robust method, widely used for the preparation of several catalysts,[30] only a limited number of examples employed SC for electrocatalytic OER[31-33] and, to our surprise, self-supported water splitting electrocatalysts produced by solution combustion are absent in the literature.[34]

This work demonstrates that solution combustion synthesis can serve to achieve rational design, applicability, and improved understanding at the atomic level. Indeed, in contrast to the classical thermal approaches as nitrate decomposition methods, SC guarantees a wide range of chemical manipulation and tunability because of the presence of a fuel.[12-14] Under the proper stoichiometric fuel-to-oxidant ratio, at the ignition temperature, the self-combustion propagates with a copious amount of gas evolution, affording foamy and porous materials with an enhanced surface area. Furthermore, the targeted product and composition can be rationally designed by merely introducing a foreign cation in a controlled manner to prevent phase segregation of the final material.[35] SC can be used to prepare metal oxides,[36-38] and in pioneering work by Marks, it has been demonstrated to grow transparent conductive oxides on glass slides.[39] Therefore, we proposed to combine the advantages of solution combustion with the ones obtained in self-supported catalysis, merging the benefits from the two different approaches.[38]

Herein, we reported the use of SC to generate self-supported NiO and metal-doped NiO on nickel foam (where the dopant metals are introduced as Mn(II), Fe(III), Co(II) and Zn(II) precursor salts). The as-prepared electrode materials exhibit excellent

performances in terms of robustness (consecutive chronopotentiometry and accelerated degradation tests), accompanied by extraordinary low overpotentials at 10 mA/cm^2. For instance, $Fe_{0.1}$-NiO afforded a η_{10} of 234 mV, which decreased to 190 mV upon increasing Fe content in NiO up to 40% ($Fe_{0.4}$-NiO) at pH 13. Those performances outperform those benchmark self-supported NiFe oxides obtained by other methods, which ranges between 250 mV to 220 mV at pH 14.[40-42] We not only reveal that the fuel plays a fundamental role in enhancing the electrochemical surface area, but that can be used to introduce different cations to modulate the intrinsic properties of the catalysts. Spectroelectrochemical (SEC) analyses combined with electrochemical impedance spectroscopy (EIS) allowed us to determine the spectra of the reactive intermediates accumulated during OER and conclude that a similar intermediate is observed for each doped catalyst. The stark difference in performance is instead assigned to the earlier onset of accumulation of these intermediates in the Fe-, Mn- and Co-doped NiO samples compared to the undoped material. This trend is also consistent with the specific capacitance observed by impedance spectroscopy, thereby suggesting that these dopant metals aid the formation of oxidized species responsible for the high (electro)catalytic activity.

Synthesis, deposition and characterization of NiO and M-NiO. Both NiO and M-NiO have been synthetized via one-pot solution combustion (SC) synthesis (Figure 1 and SI):

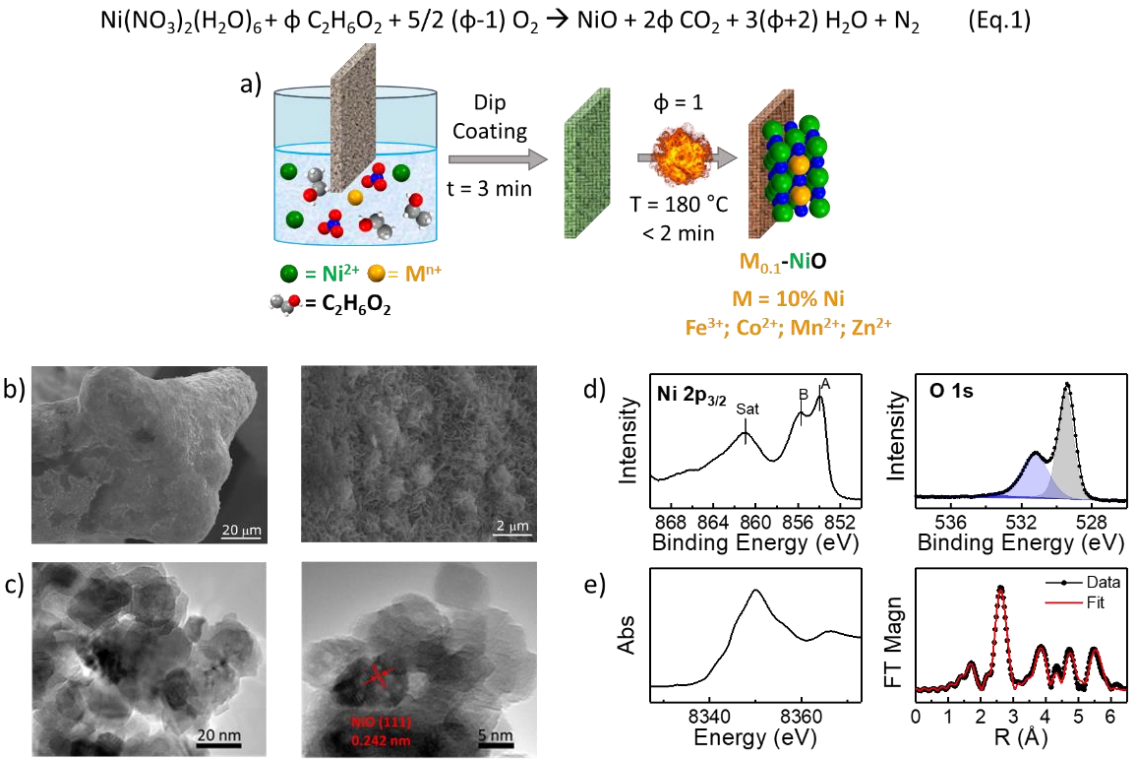

Figure 1. Top equation: general stoichiometric relationships for the synthesis of NiO and M-NiO. For the synthesis, $Ni(NO_3)_2(H_2O)_6$, $M^{n+}Cl_n$ (M = Mn, Fe, Co, Ni, Zn) and ethylene glycol (EG) were used as a source of Ni, dopant metal cation (10% unless otherwise specified), and coordinating agent and fuel. The powders synthetized respond to the general formula $M_{0.1}$-NiO. a) Illustration of the synthetic path for NiO and M-NiO grown directly onto NF, consisting in a succession of dip coating (room temperature, 3 min) and then combustion of the impregnated NF. b) Represent SEM and c) STEM images of as-deposited catalyst for NiO at different magnification levels. d) Shows Ni $2p_{3/2}$ XPS spectrum (left) with characteristic peaks exhibiting the nonlocal (A) and local (B) screening contributions to the main peak and a charge-transfer satellite, as well as the O 1s (right) showing a contribution associated to lattice oxygen and adsorbed oxygenated species. e) Characteristic XANES (left) and EXAFS (right) for NiO.

When the reactive mixture is heated up, a fast shock exothermic reaction occurs between the oxidant (NO_3^-) and fuel (EG), according to the stoichiometry reported in the equation of Figure 1. The optimal oxidant-to-fuel ratio (ϕ) was found to be 1 and the synthesis produces the desired phase cleanly without the need for external oxygen (Eq. 1, Figure S1). The reaction was also carried out directly on nickel foam (NF, 1 x 2 cm^2), resulting in a functionalized electrode after intensive sonication in water. When the reaction is

carried out in the presence of the dopant salts, the cation inclusion was confirmed to be ~10% using ICP-OES analysis (Table S1).

The electrode surface and composition were analysed employing scanning electron microscopy (SEM), scanning transmission electron microscope (STEM) and X-ray Photoelectron Spectroscopy (XPS) (Figure 1b-1d). The micrographs show that the support is fully covered by the material, although the catalyst tends to accumulate at NF surface defects, probably because the strong sonication process removes weaker bonded material. In general, the morphology is foamy, characterized by laminar, vertically aligned structures of hundreds of nanometres, generated by the large quantity of gas released during the combustion (Figure S2-S3). At higher magnification, the materials appear as porous solids consisting of randomly assembled near-spherical or irregular isotropic grains. The irregular shape of those particles can be clearly observed in TEM and STEM. The nanoparticles of Fe-, Mn- and Co- doped samples are in general thin, in sharp contrast with undoped and Zn- NiO. No additional evident differences were noticed between as-prepared materials as showed in the Figures S4-S5-S9. At STEM resolution we also observed the lattice fringes of NiO with an interplanar distance of 0.242 nm, corresponding to (111) plane of NiO.

Further surface characterization was performed by X-ray Photoelectron Spectroscopy (XPS), indicating the presence of mainly Ni^{2+} and oxygen from the lattice corresponding to NiO. At the same time, at the surface, Ni^{3+} was also detected, and in a higher amount in doped NiO electrodes compared with the undoped NiO (Figure 1d, Figures S6 and further details in Figure S7). Such an increase in Ni^{3+} surface concentration can be associated with a higher amount of surface defects upon doping. Consistent with the previous observation, where the incorporation of dopants produces a deviation in the

stoichiometry and lattice distortion in NiO that may favour the formation of surface defects.[43, 44]

On the other side, the bulk of the material was characterized by PXRD, which indicates the formation of NiO rock salt phase for all M-NiO samples, confirming that no phase segregation occurs (Figure S8a). Furthermore, attenuated total-reflectance infrared spectroscopy (ATR-IR) (Figure S8b) showed vibrational modes between 400 cm^{-1} and 600 cm^{-1}, which can be attributed to the stretching modes of the Ni-O vibrations.

The bulk of synthesized materials were further characterized by X-ray absorption spectroscopy at both the Ni and dopant metal K-edges (Figure S10-S11). The Ni K-edge XANES profiles are consistent with previously reported nickel oxides, with EXAFS analysis showing a first shell Ni-O scattering distances at ~2.07 Å, Ni-Ni scattering distances at ~2.95 Å as well as higher shell scattering as expected from NiO_x.[45-47] The NiO matrices exhibit a rising edge of the XANES spectrum with half-height energy centered at 8341.5 eV (Table S2) and a pre-edge at 8332.1 eV, having a normalized intensity of 0.06, indicating a Ni^{2+} oxidation state in a N/O octahedral environment.[48] The apparent discrepancy with the observed Ni^{3+} by XPS can be easily explained by the different sampling depths of the two techniques.[49] Interestingly, the inclusion of dopant metals does not significantly affect the XANES region of the spectra, suggesting that, at least, the local Ni center environment is unaffected by the dopant. However, clear differences are observed in the Fourier transformed (FT) EXAFS spectra upon doping, particularly for Fe and Mn. These samples presented a decrease in the intensity of the FT features above 2 Å, suggesting a perturbation of the long-range NiO_x lattice (Figure S15-S16). Effectively the result is a drop in the coordination number of the second M-M and higher scattering shells and correlates with the decrease in particle size as detected in TEM and PXRD (Table S3 and Figure S9).[50] However, theory predicts EXAFS should

not distinguish differences from bulk in particle sizes larger than 4 nm as is the case here.[51] Taken together with the information from SEM analysis, PXRD and XPS, this points to the formation of defects within the lattice structure/surface. Marked differences are also evident from the dopant metal K-edges. While the Co K-edge XANES spectra (Figure S11 and Figure S14) indicate Co^{+2} octahedral centres,[52] spectra of Fe-NiO and Mn-NiO (Figure S11, Figure S15 and Figure S16) are consistent with a +3 oxidation state for both Fe and Mn centres.[53-55] This indicates a change in oxidation for Mn from +2 to +3 during the combustion. Furthermore, while Co has a similar EXAFS profile to the Ni centres (Figure S14), suggesting that Co is embedded in the NiO_x matrix, the low ligancy of the Fe (Figure S15) and Mn (Figure S16) dopants both in the first M-O shell at and M-M shells suggest these latter are formed on the surface of the NiO_x matrix.[26]

Electrocatalysis at pH 13.

First, to prove the benefits of the electrocatalytic materials obtained by the solution combustion method, we benchmarked our new $Fe_{0.1}$-NiO *in-situ* grown on nickel foam by solution combustion (labeled only $Fe_{0.1}$-NiO) against drop-casted $Fe_{0.1}$-NiO (labelled $Fe_{0.1}$-NiO_DC) also obtained by SC. We also compared the $Fe_{0.1}$-NiO grown on NF by SC with the classical decomposition method that does not involve a fuel. Thus, the same $Fe_{0.1}$-NiO system was prepared by thermal nitrate decomposition (TND) self-supported on NF, accordingly to the literature reports.[12, 14]

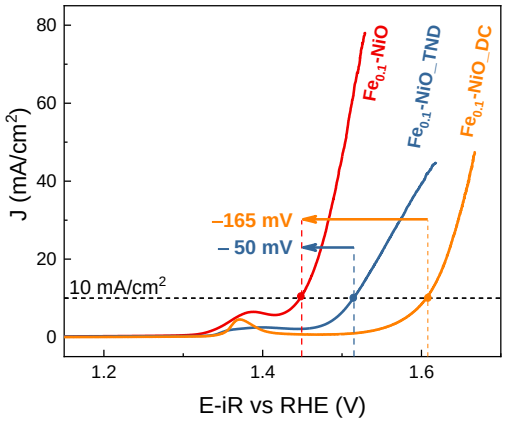

Figure 2. Comparison of a linear sweep voltammetry (at 2.5 mV/s, pH 13) $Fe_{0.1}$-NiO *in-situ* grown (red line) on NF by SC or drop-casted (orange line) and thermal nitrate decomposed $Fe_{0.1}$-NiO (blue line) on NF. The overpotential gain at 10 mA/cm^2 is also indicated in the figure.

The catalytic performances of drop-casted $Fe_{0.1}$-NiO_DC are quite poor. Nevertheless, when the same catalyst is grown on NF, a tremendous improvement of the performances is observed. At 10 mA/cm^2, the overpotential for self-supported $Fe_{0.1}$-NiO is 165 mV lower than the drop-casted sample (Figure 2). Analogous results can be systematically observed for the other M-NiO_X (see Figure S18). On the other side, the LSV of thermally decomposed $Fe_{0.1}$-NiO-TND sample has an overpotential at 10 mA/cm^2 (η_{10}) of 283 mV, in line with other reports,[12] that is 50 mV higher than the analogous combustion counterpart (Figure 2). As showed by SEM analysis, the morphology of obtained samples is radically different. $Fe_{0.1}$-NiO-TND exhibits a dense surface, characterized by low electrochemical surface area (ECSA), as previously observed for thermally decomposed materials without added fuels[12] (see Figure S19a for SEM pictures and Figure S20 for ECSA determination). On the other hand, the SC-prepared $Fe_{0.1}$-NiO presented a foamy nature, higher electrocatalytic surface area, and therefore, increasing the number of active sites, while the morphology facilitates product diffusion and gas release (Figure S19b). However, the intrinsic catalytic activity is the same for both after scaling the current

density by the ECSA, as expected for catalysts with the same chemical composition but obtained by different preparation method (Figure S20c).

Encouraged by the effectiveness of SC over conventional approaches, we studied the doping in M-NiO samples. We found that the activity is modulated by the nature of the dopant cation, following the order $Fe_{0.1}NiO$ >> $Co_{0.1}NiO$ > $Mn_{0.1}NiO$ > $Ni_{0.1}NiO$ > $Zn_{0.1}NiO$ (Figure 3a). The overpotentials at 10 mA/cm^2 (η_{10}) are: 234 mV, 285 mV, 321 mV, 351 mV and 362 mV, respectively. Such a trend fits well with the charge-transfer resistance (R_{CT}) during OER, measured employing impedance spectroscopy (EIS) (Figure S21b and Table S4). Analogously, the Tafel slopes (Figure 3b) increases from $Fe_{0.1}$-NiO (64 mV/dec), to $Co_{0.1}$-NiO (ca. 105 mV/dec), $Mn_{0.1}$-NiO (ca. 105 mV/dec), NiO (125 mV/dec), with the highest slope belonging to poorly active $Zn_{0.1}$-NiO (168 mV/dec). Results from both EIS analysis and Tafel plot suggest the increase in activity obtained upon doping derives from a more effective charge transfer during the OER.

To evaluate the robustness of the electrodes, the electrochemical performances were evaluated under conditions aimed to stress the material. These consisted of a sequence of chronopotentiometry measurements at 10 mA/cm^2 over 24 hours, followed by an Accelerated Degradation Test (ADT) consisting of 2500 CV. Chronopotentiometry at 10 mA/cm^2 produced O_2 with unitary Faradaic efficiency (Figure 3c and Figure S22 for on-line GC measurements), at the end of which the ECSA slightly increased (Figure S23-S26 and Tables S5). Consequently, in the case of $Fe_{0.1}$-NiO, $Co_{0.1}$-NiO and $Mn_{0.1}$-NiO, the overpotential at 10 mA/cm^2 (η_{10}) decreased after the long-term chronopotentiometry, and remained unaltered after accelerated degradation test experiments, demonstrating great robustness (Figure S27). Conversely, NiO and $Zn_{0.1}$-NiO basically show unaltered activity, with traces of Zn leaching detected in the electrolyte solution (see ICP-OES Table S6 for details).

In order to assess the intrinsic activity, the LSVs were normalized with the ECSA (Figure 3d). The double layer capacitance was independently estimated by EIS and CV methods. As listed in Table S5, the highest double layer of 28 mF cm^{-2} belongs to $Mn_{0.1}$-NiO, followed by Co (25 mF/cm^2), Fe (18 mF/cm^2), NiO (12 mF/cm^2) and finally Zn-NiO (10 mF/cm^2). Surprisingly, the catalyst with the highest capacitance (and therefore the maximum ECSA) is not the best-performing one. Therefore, the ECSA-normalized LSVs (Figure 3d) evidence a significant disparity in the intrinsic activity, suggesting that, despite the lower number of active sites, Fe cation exerts a high beneficial effect in catalysis delivering 0.6 mA_{ECSA}/cm^2 at only 290 mV of overpotential.

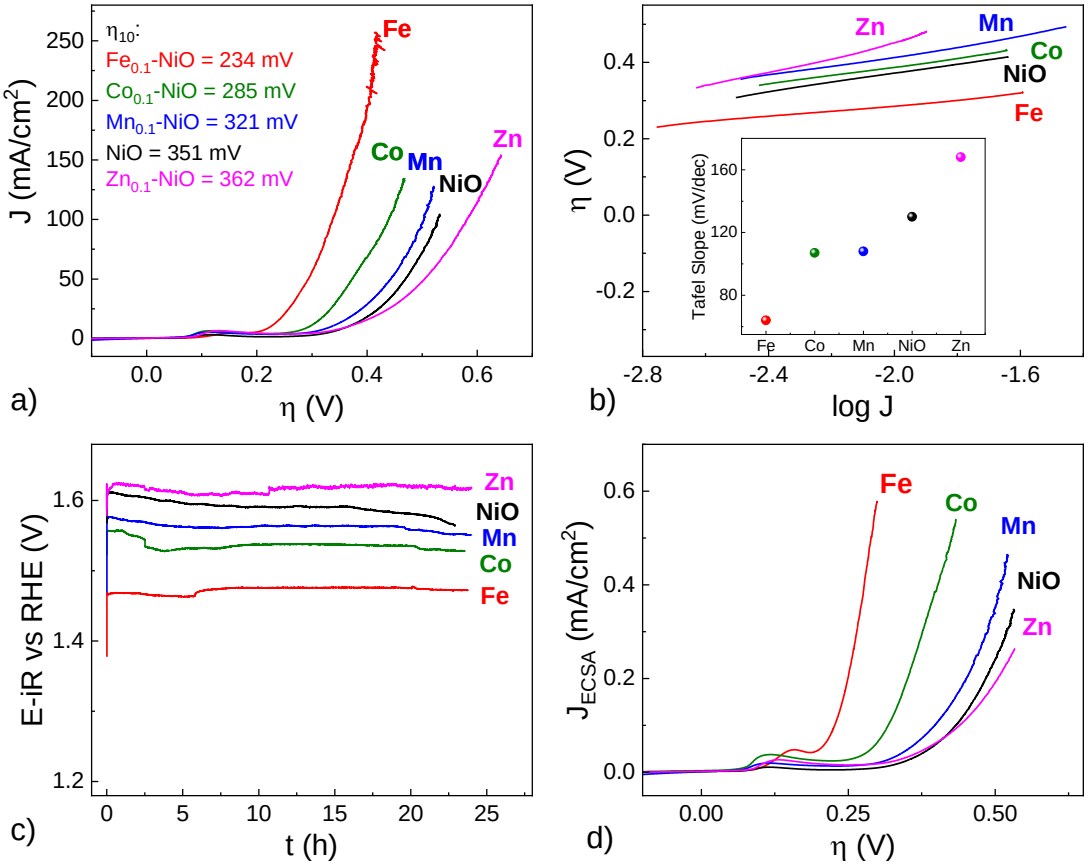

Figure 3. Panel a) Comparison of the LSV curve (recorded at 2.5 mV/s) for all the samples, b) Tafel plots, with the value of the Tafel slope for each dopant material in the inset, c) Long-term chronopotentiometric (CP) experiments during 24 hours at 10 mA/cm^2, d) ECSA-normalized LSV curves for all the samples. In all the graphs, Fe is

represented in red, Co is green, Mn blue and Zn magenta. The electrolyte consists of a solution of KOH, pH 13.

A fair comparison with the benchmark catalysts in the literature is reported in Table S7. In particular, it is noteworthy to focus on the best-performing $Fe_{0.1}$-NiO, which is able to deliver 10 mA/cm^2 at a record overpotential of only η = 234 mV after 24 hours chronopotentiometry and 2500 ADT cycles. This value alone breaks the previous $NiFeO_x$ benchmark reported by Cui e*t al.* (η_{10} = 250 mV in 1 M KOH) and is quite impressive for only 10% Fe-doped NiO working at pH 13. As such, we also study the inclusion of Fe in the NiO rock salt phase using the same methodology. The new materials synthetized still show the sole NiO phase (Figure S28a) until Fe doping of 40%. Above this value, the diffraction patterns (Figure S28b) clearly indicate a phase transition from NiO to a spinel based AB_2O_4 (with A represents the divalent tetrahedral cation (Ni^{2+} or Fe^{2+}) and B is the octahedral Fe^{3+}). The new spinel samples correspond to the formula $Ni_XFe_{3-X}O_4$, where the Ni is the host cation for iron oxide. No other phases are detectable, confirming the versatility of the method for produce single crystalline phases. In the Fe-doped NiO samples, the increased iron content further improves the already notable performances observed (Figure S29a). In particular, the catalyst containing 40% of Fe shows an extraordinarily low water oxidation overpotential of 190 mV at 10 mA/cm^2 (Figure 4). To the best of our knowledge, this is the first time that a simple metal oxide electrocatalyst displays such outstanding activity at pH 13 (Figure 4 and Table S7).[40, 56-61]

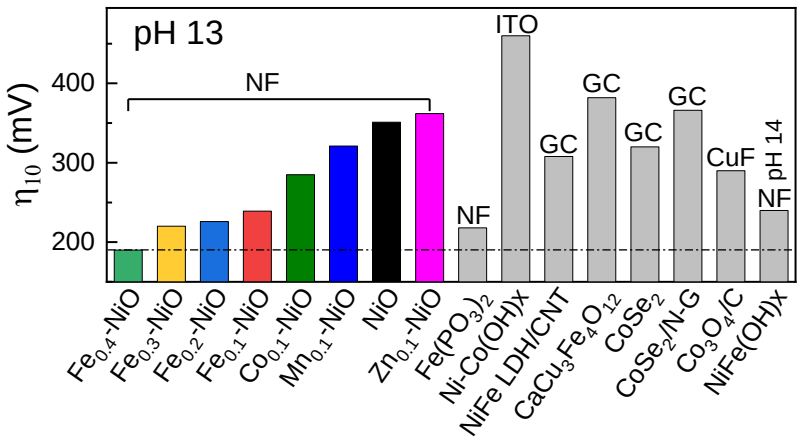

Figure 4. A comparison in the η_{10} at pH 13 with reported benchmark in the literature.

Instead, the phase transition occurring for Fe > 40% is not beneficial for the catalytic activity (Figure S29b). This is in line with several reports which assess the best Fe content around 30-40%.[62] The Ni-doped Fe_3O_4 catalysts exhibit poor performances, suggesting that the formation of discrete spinel iron oxide phase disfavours the activity.

As corroborated by the TOF calculation (Figure S30a, obtained from the total mass loading, Figure S17a), the pure phases NiO and Fe_3O_4, exhibit low TOF values (0.06 ms^{-1} and 2.6 ms^{-1}, respectively). Instead, upon cation doping there is a clear synergistic effect of the presence of both metals. For Fe-doped NiO samples, the TOF_{Fe} is systematically higher than TOF_{Ni} (Figure S30b). This finding is in line with previous papers[63] reporting that the FeOOH active phase has remarkable intrinsic activity but suffer of poor conductivity.[64] For this reason, the inclusion of Fe in a conductive MOOH host (as Ni) enhances the performances of the overall catalyst. Our conclusions point that until Fe is entropically distributed in the NiO lattice it can boost the OER performances, instead when discrete Fe-based material is formed, the activity is depressed.

We postulate that such outstanding performances emerge from a combination of two main factors: the self-supported nature of the catalysts, which offer superior adhesion and stability on the current collector, avoiding the use of any binder which may introduce

additional resistance losses and the porous morphology of the material, which lead to a maximization of the number of active sites, as witnessed by the high ECSA.

Mechanistic Insights by XPS, UV-Vis SEC and EIS.

To shed some light about the nature and the amount of the active species we combined electrochemical studies with structural characterization based on PXRD, SEM, STEM, Raman and XPS, performed before and after OER. As mentioned, the performances improve during OER tests, as a consequence of the increment of ECSA. Nevertheless, the diffraction pattern is unaltered before and after catalysis (Figure S31), indicating that the bulk of the material maintains its structural integrity, in good agreement with the observation in STEM (Figure S32), where no changes in the lattice distances are observed, and SEM (Figure S33). Ex-situ Raman characterization reveals only small surface changes for $Fe_{0.1}$-NiO after OER (Figure S34). Before catalysis, the sample showed vibrational modes at 560 cm^{-1} associated to Ni-O streching modes[65] and 680 cm^{-1}, related to Fe-O modes.[66] This latter showed a clear enhancement after catalysis. XPS provides conclusive evidences for the formation of M-NiOOH species (Figure S35), showing an evident increase of both the Ni^{3+} concentration and hydroxyl species on the surface, suggesting the inclusion of an OH group into the metal coordination sphere.[46, 67, 68] Therefore, the increment of the ECSA reflects the increasing concentration of charged species at the surface and the formation of M-NiOOH active species from the pre-catalytic NiO phase.[69, 70]

Nevertheless, to quantify the active sites, we replaced NF for fluorine doped tin oxide (FTO), owing to negligible substrate capacitance in comparison to NF (which dominated the capacitance response, as observed in the EIS spectra, Figure S21) and its transparency, which is critical to perform spectroelectrochemical experiments. To this aim, we plated

NiO and its doped M-NiO derivatives *via* conventional spray coating of metal oxides dispersions.

The reactivity order in FTO remains the same as that observed on NF (Figure 5 and Figure S36), with the ECSA-normalized resistance (Figure 5b) that conveys the information on water oxidation kinetics (charge transfer resistance) and the Tafel slopes having nearly identical values (Figure S37) to those discussed in NF.

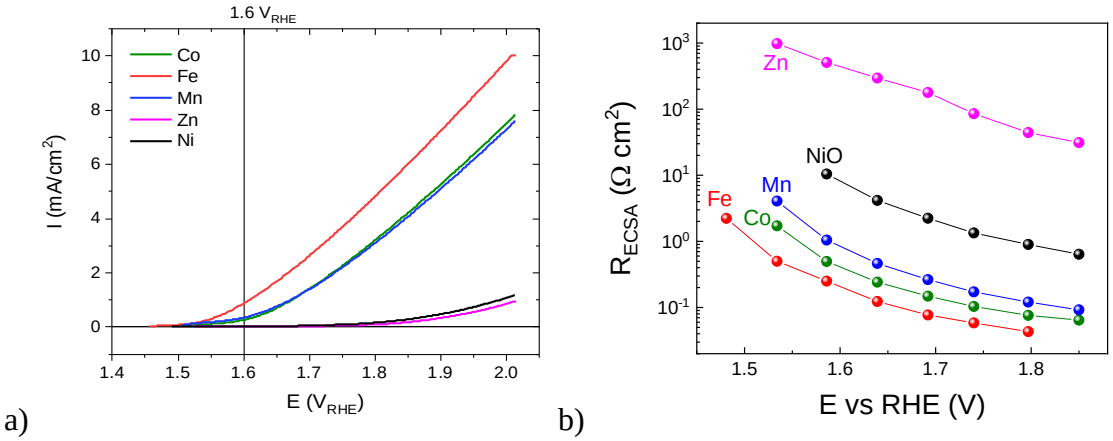

Figure 5. Performance comparison between all the (M)-NiO materials on FTO in KOH pH 13. Panel (a) shows linear sweep voltammograms measured at 10 mV/s. Panel (b) shows the reduction trend in the ECSA-normalized charge transfer resistance as a function of the applied potential.

Interestingly, the position of the Ni redox waves and their corresponding integrated charge (that in NF cannot be analysed) are strongly influenced by the metal dopant, suggesting an homogeneous distribution of the dopant in NiO lattice and a strong electronic coupling between them.[71] Since this redox process has been attributed to the conversion from Ni^{2+} to Ni^{3+}-(O)OH active species,[72, 73] the peak position and its magnitude indicate the easiness of the hydroxyl binding on the electrode surface. As shown in Figure S38, the $Mn_{0.1}$-NiO possesses the highest integrated charge and the earliest peak position of the series, followed by Co, Fe, NiO and Zn, suggesting higher

conversion of the Ni^{2+} to the active species, again in agreement with the trend of the ECSA in NF.

In the same line, further electrochemical characterization performed by EIS reinforces the overall picture (Figure S40 and Table S8). The observed features in the capacitance versus the applied potential (Figure S41a) are characteristic of NiO_x catalysts, as it has been recently published.[74] Moreover, we performed Mott-Schottky analysis (MS) at the most cathodic potentials to determine the carrier density (Figure S42) and the value of the flat band potential (E_{FB}) (Table S9).[75] In the pre-catalytic region ($V < V_{onset}$), MS plot shows a negative slope, indicating p-type semiconductors, as previously reported for NiO_x.[76-78] The p-doping in OER catalysis is supposed to exert a beneficial effect on catalysis because positive charges promote the adsorption of negatively charged intermediate species as O*, OH* and OOH*, which play a key role on OER.[79, 80] Specifically, the MS slope is more negative for $Mn_{0.1}$-NiO and becomes more positive for Co-, Fe-, undoped and $Zn_{0.1}$-NiO, matching the trend discussed about the Ni^{2+} redox peaks (Figure S43a). Instead, the E_{FB} matches the reactivity trend, being more positive for $Fe_{0.1}$-NiO and shifting towards anodic potentials as the activity decreases (Figure S43b and Table S9). The match between the Mott-Schottky slope and the position of the Ni^{2+} redox peaks (Figure S43) make us think that the p-character can be thought as an indicator, in the pre-catalytic region, of the OH binding strength in the Ni^{3+}-(O)OH species. With this idea in mind, we argue that affinity of $Mn_{0.1}$-NiO toward the OH binding is the strongest, resulting in the formation of a very stable $Mn_{0.1}$-NiOOH intermediate. Consequently, the catalytic onset shifts towards more anodic potentials (as well as the E_{FB}). As the OH affinity and the consequent stabilization decreases (i.e. for in Co- and Fe- samples) the E_{FB} and the catalytic onset become more cathodic. Instead, undoped NiO and Zn-doped

sample with poor p-character are less prone to get oxidized to Ni^{3+}(O)OH, and therefore do not efficiently catalyse O_2 evolution.[79]

To gather more information about the nature and density of these accumulated species, we examined the catalytic region by UV-Vis spectroelectrochemistry (UV-Vis-SEC). We note that although UV-Vis-SEC were measured for samples prepared by spray-coating to obtain a homogenous coating, the spectral features are similar to those obtained on samples prepared directly by solution combustion synthesis (Figure S45). Figure 6a shows the absolute change in absorption at 500 nm (λ_{max} for each catalysts). Since the absolute changes in the absorption spectra vary by more than an order of magnitude (Figure S46), normalized spectra better illustrate their similar shape (Figure 6a, inset). This similar feature suggest that the accumulated reactive intermediate is analogous for all of them, independently of the dopant nature. This may be considered as an indication that a Ni-based intermediate accumulates before the rate-determining step, as previously observed in the spectroelectrochemical analysis of NiOOH with <10% Fe doping.[81] While the spectra of the accumulated intermediates are similar for each catalyst, the magnitude of the SEC signal at the same applied potential is quite different. $Mn_{0.1}$-NiO shows the largest signal amplitude, likely indicating the greatest density of reactive intermediates, followed by $Co_{0.1}$-NiO and $Fe_{0.1}$-NiO, whereas NiO or $Zn_{0.1}$-NiO only produce a small signal.

Interestingly, this is the same trend observed in the ECSA-normalised capacitance data measured in the catalytic region (Figure 6b inset), which reveals a higher accumulation of charge for $Mn_{0.1}$-NiO, followed by $Co_{0.1}$-NiO, $Fe_{0.1}$-NiO, NiO and $Zn_{0.1}$-NiO. This also correlates well with the catalytic onset potentials observed in Figure 5a, demonstrating a clear relation between the facile accumulation of these reactive intermediates observed and the relative ease of the current generation.

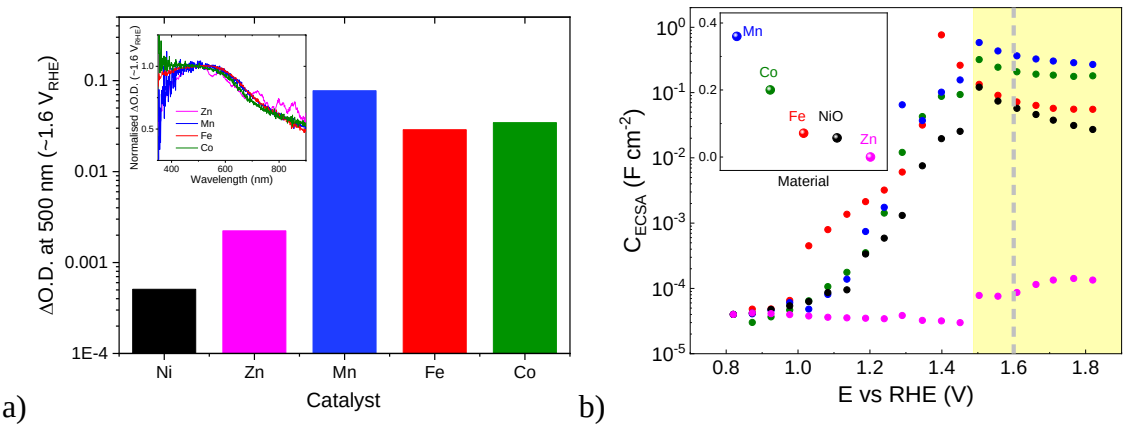

Figure 6. (a) Amplitude of spectroelectrochemistry signal at 500 nm for each electrocatalyst at ~1.6V_{RHE}. Inset shows normalized signals for each doped catalyst (the undoped NiO signal gave too small a signal-to-noise ratio to compare). (b) Capacitance normalized by ECSA as a function of applied potential for the different M-NiOx/FTO samples. Shaded yellow area corresponds to the catalytic region and the inset shows the trend in the capacitance, normalized by ECSA at 1.6 V_{RHE} (dashed grey line).

All this information reinforces the analysis in the precatalytic region, pointing that the dopant plays a crucial role in stabilizing the active species. In this sense, the accumulation of a high number of intermediates for $Mn_{0.1}$-NiO reflects an inefficient kinetics for water oxidation, whereas the poor accumulation of $Zn_{0.1}$-NiO accounts for its scarce reactivity with the key intermediates of OER. However, in-depth kinetic and mechanistic studies are currently on-going to validate such hypothesis and will be separately published.

Conclusions.

In summary, we have found a simple and effective solution combustion-based approach to grow NiO and M-NiO catalysts (M = Fe, Co, Mn, or Zn) on nickel foam. We showed that the method allows a wide catalyst composition tunability. The as-prepared electrodes exhibited outstanding performances with large electrochemical surface area and excellent stability. In terms of overpotential, all the electrodes tested overperformed the corresponding benchmarks. Among all the catalysts tested, the best performing NiOx catalysts were those doped with Fe. The overpotential to drive OER at 10 mA/cm^2 was

decreased from 239 mV to 190 mV as a function of the Fe-content (from 10% to 40%), representing a new benchmark for metal oxide electrocatalysts in 0.1 M KOH. Finally, spectroelectrochemical (SEC) and electrochemical impedance spectroscopy (EIS) techniques helped to rationalize the role of the metal dopant cation. Our finding indicate that the dopants modulate the intrinsic hydroxide affinity of NiO, which determines the extent of the conversion of the initial NiO phase to M-NiOOH active species. However, strong interaction results in lower catalytic activity, whereas weak binding inhibits the formation of the active species.

In conclusion, we expect that the straightforward preparation of effective self-supported metal-oxide catalysts on electrodes and the possibility to study them provides a platform for developing further highly efficient electrocatalytic materials.

Methods

Synthesis of undoped NiO. Undoped NiO was synthetized in one-pot SC synthesis by mixing in 10 mL of MilliQ water 350 mg of $Ni(NO_3)_2(H_2O)_6$ with ethylene glycol (67 μL) for a final metal concentration of 0.12 M. The combustion mixture was stirred for 1 h before transferring inside a muffle furnace. Two gradients temperature where applied: an initial fast ramp of 10 °C/min up to 100 ºC, followed by a slower one of 2 °C/min, until a final T = 350 ºC was reached. Only 5 minutes of soaking connects the two ramps, whereas, at the end of the second, the sample was allowed to stay for 1 hour.

Synthesis M-NiO. This synthesis was repeated identically to that of NiO, but this time to the combustion mixture, 10% of $M^{n+}Cl_n$ was added. In particular, a solution 0.24 M of the dopant salt was prepared by dissolving the corresponding precursor in ultra-pure water and 500 μL of this solution were injected in the vial containing Ni^{2+}/EG precursors (0.12 M, 10 mL).

Synthesis NiO@NF and M-NiO@NF. Two equimolar solutions (0.5 M) of $Ni(NO_3)_2$ and $M^{n+}Cl_n$ were separately prepared. EG was added to the Ni solution in order to obtain a 1:1 metal-to-fuel

ratio. Finally, the Ni and EG solution was mixed with the dopant one in the desired ratio (from 9:1 to 3:2) in order to keep the final metal concentration at 0.5 M. The new solution was allowed to stir one hour before a pre-cleaned piece of NF was dip-coated in combustion vial. For dip coating, NF was immersed 180 seconds into the combustion mixture and successively removed from the vial and transferred in a flat porcelain crucible. The latter was then placed into a pre-heated muffle furnace at 180 °C during 2 min to allow the combustion to occur. The as-prepared electrode was rinsed with abundant ultra-pure water and sonicated for 30 seconds in acetone, before dried under a nitrogen stream.

Material Characterization. Powder X-ray diffraction (PXRD) patterns of (M)-NiO powder samples were recorded on a D8 Advance Series 2Theta/Theta powder diffraction system using CuKα1-radiation in transmission geometry. The data were collected with an angular step of 0.02° at 12 s per step and sample rotation. Fourier-Transformed Infrared measurements were carried out on a Bruker Optics FT-IR Alpha spectrometer equipped with a DTGS detector, KBr beamsplitter at 4 cm^{-1} resolution using a one bounce ATR accessory with diamond windows. Scanning Electron Microscopy (SEM) conditions are 20kV accelerating voltage and working distance close to 10 mm. Transmission electron microscopy (TEM) operated at 80 kV. Samples were dispersed in ethanol and a drop of resultant suspensions was poured on carbon coated-copper grids. XPS spectra were recorded using a SPECS NAP-XPS System incorporating the DeviSim NAP reaction cell. The spectrometer is equipped with a Al Kα monochromated source (hν = 1486.6 eV) operating at 50 W (1.68 mA emission current and 13 kV) with a 300 μm^2 x-ray spot. Binding energy calibration was made using Au 4f7/2 (84.01 eV), Ag 3d5/2 (368.20 eV) and Cu 2p3/2 (932.55 eV). Samples for metal K-edge X-ray absorbance were measured in fluorescence using a 36 element Ge detector as FTO-plated samples accordingly to the procedure described below. Measurements were taken at 25 K using a liquid helium cryostat and a Si(220) double crystal monochromator. The Athena software package was used for data calibration normalization and EXAFS data extraction. Energies were calibrated to the first inflection point of metal foils, taken as 6539 for Mn, 7111.2 for Fe, 7709.5 for Co and 8331.6 for Ni. For EXAFS analysis.

Electrochemistry

Electrodes preparation. The deposition technique depends on the support: SC was used for NF (20 x 10 x 0.9 mm^3) and spray coating for FTO (25 x 10 mm^2). In both cases, the geometric surface area was fixed to 1 cm^2. For the spray coating, 5 mg of the catalyst were dispersed in 1 mL of a solution of 987 μL of EtOH/H2O (3/1) and 12.7 μL of FAA Fumatech anionomer (ca. 10% w/w respect to the catalyst). Four coatings of 125 μL each (for a total of 500 μL) of such a dispersion were sprayed with an airbrush onto an FTO glass slide – preheated at 75°C – whose surface was entirely covered by a Kapton tape, except an exposed area of 10 x 10 mm^2.

Electrochemical Tests. For electrochemical tests, a standard sequence of experiments was used for each catalyst, involving an initial CV (10 mV/s) of 3-6 cycles, until the electrode was stabilized, then linear sweep voltammograms (LSVs) were run with a scan rate of 5mV/s. All the voltammetry experiments were corrected, accounting for ohmic loss iR, determined by electrochemical impedance spectroscopy (EIS). EIS experiments were conducted in the potential window 1– 2 V vs RHE and a frequency range between 300 kHz and 0.1 Hz with an AC amplitude of 15 mV. TOF_{redox} values were calculated according to the formula:

$TOF_{redox} = \frac{J_{geom}}{4q}$, where q is the integrated charge of the cathodic Ni redox wave.

The ECSA was determined by sweeping the potential in a 0.1 V window around the OCP at different scan rates (1 mVs^{-1}; 2.5 mVs^{-1}; 5 mVs^{-1}; 10 mVs^{-1}; 15 mVs^{-1} and 20 mVs^{-1}). The vertex potentials were held for 10 seconds before starting the reverse scan. The values of the anodic and cathodic currents were then plotted as a function of the scan rate and from the linear fit, the values of C_{DL} are obtained for different catalysts. The ECSA is then obtained by dividing the C_{DL} by the specific capacitance (40 μF/cm^2).

Impedance Spectroscopy. The EIS raw data were fitted using EC-Lab software. Nyquist plot appearance depends on the system studied. In general, two semicircles appear, so the impedance response is described by the Armstrong-Henderson equivalent circuit,

otherwise, a simple Randles' circuit was used. In any case, a constant phase element (CPE) was used to accounts for the deviation from the ideal behavior of a capacitor.

Mott-Schottky analysis was carried out using the expression:

$\frac{1}{C_{SC}^2} = \frac{2}{\varepsilon_0 \varepsilon_r e N_A A^2}\left(\phi_{SC} - \frac{kT}{e}\right)$, where $\phi_{SC} = V - V_{FB}$

C_{SC} represents space charge capacitance, e is the elementary charge, ε_0 is the permittivity in vacuum, ε_r is the relative permittivity of NiO_x, (taken as 9.1)[82], N_A is the acceptor density, A is the area, k is the Boltzmann constant and T is the absolute temperature, taken as 298 K. From this analysis, the values of the flat-band potential (V_{FB}) and the acceptor density (N_A) were extracted.

Faradaic Efficiency. On-line analysis of the gas mixture during long-term CP experiment was performed by connecting the electrochemical cell to a micro-GC (Agilent 490 micro gas chromatograph, equipped with a thermal conductivity detector and a Molesieve 5Å column). O_2 was almost fully removed from the electrolyte using a constant N2 flux of 30 mL/min (fixed with a mass-flow controller, Alicat®). During the CP experiment, the GC autosampler withdraws an aliquot of the headspace each 10 min, during at least 4 hours. The amount of O_2 and H_2 in moles was determined by the following equation:

$mol\ gas = \frac{[(I - I_0)I_{Cal}]Ft}{V_m}$, where I is the measured signal, I_0 is the initial value of the signal (in the case of O_2 it is the residual amount of oxygen in solution), I_{Cal} arises from the calibration, F is the flux (0.03 L/min), t is the time, whereas V_m is the molar volume (22.414 L/mol).

Acknowledgements

The authors acknowledge financial support of the ICIQ Foundation, the European Research Foundation for H2020 projects ERC-2015-CoG GREENLIGHT_REDCAT 648304, (J.L.-F.), ERC CoG HyMAP 648319 (V.O.), H2020-FETPROACT-01-2016 A-LEAF (S.C., R.R., J.R.D., M.G.-T., S.G., A.B., J.L.-F.), MINECO (CTQ2016-80038-R, J.L.-F.) and MICINN (PID2019-110050RB-I00, J.L-F.) and AGAUR 2017-SGR-1647 (J.L.-F.), Ministerio de Ciencia,

Innovación and Universidades of Spain (project ENE2017-85087-C3-1-R, S.G./M.G.-T.) and Spanish AEI-MINECO/FEDER Nympha Project (PID2019-106315RB-I00). Also, has been funded by the regional government of "Comunidad de Madrid" and European Structural Funds through their financial support to FotoArt-CM project (S2018/NMT-4367). Besides, Fundacion Ramon Areces funded this work through ArtLeaf. We would like to thank the support of the SAMBA beamline at the SOLEIL synchrotron (France) for their support and time for data acquisition. Furthermore, we would like to thank CLAESS beamline and staff from the ALBA synchrotron (Spain) for providing reference spectra.

Author contributions

A.B. and J.L.-F proposed the idea, developed the synthetic protocol, and composed the manuscript. A.B. performed the synthesis, the general characterization of the powders, the electrochemical experiments on both NF and FTO and GC-online measurements.
M.G.-T., A.B. and S.G. designed EIS experiments and performed related data analysis. M.G.-T. performed SEM experiments on self-supported catalysts before and after OER.
S.C., R.R. and J.R.D. designed SEC experiments and performed related data analysis.
F.E.O. and V.A.P.O. designed XPS experiments and performed related data analysis before and after OER.
V.M.D., A.B. and J.L.-F. designed XAS experiments and performed the experiments and V.M.D. analysed the related data.
All authors contributed to scientific discussions and revision of the manuscript.

Present Addresses

[e] Madrid Photoactivated Processes Unit, IMDEA Energy Institute, Av. Rámon de la Sagra, 3 Parque Tecnologico de Mostoles, 28935, Mostoles, Madrid, Spain.

Competing interests

European Patent Application Number EP20382294, a patent application by A.B. and J.L.-F. was previously filed for the intellectual property described in this article.

Additional information

Supplementary information

Experimental details and methods, electrochemical data, characterization spectroscopy and microscopy, impedance spectroscopy studies, spectroelectrochemical data.

References.

1. M. S. Dresselhaus and I. L. Thomas, *Nature*, 2001, **414**, 332-337.
2. M. R. Shaner, H. A. Atwater, N. S. Lewis and E. W. McFarland, *Energy Environ. Sci.*, 2016, **9**, 2354-2371.
3. M. Grätzel, *Nature*, 2001, **414**, 338-344.
4. H. B. Gray, *Nat. Chem.*, 2009, **1**, 7-7.
5. C. Liu, J. Tang, H. M. Chen, B. Liu and P. Yang, *Nano Lett.*, 2013, **13**, 2989-2992.
6. D. G. Nocera, *Acc. Chem. Res.*, 2012, **45**, 767-776.
7. M. G. Walter, E. L. Warren, J. R. McKone, S. W. Boettcher, Q. Mi, E. A. Santori and N. S. Lewis, *Chem. Rev.*, 2010, **110**, 6446-6473.
8. P. Zhang, X. Sheng, X. Chen, Z. Fang, J. Jiang, M. Wang, F. Li, L. Fan, Y. Ren, B. Zhang, B. J. J. Timmer, M. S. G. Ahlquist and L. Sun, *Angew. Chem. Int. Ed.*, 2019, **58**, 9155-9159.
9. I. Vincent and D. Bessarabov, *Renew. Sust. Energ. Rev.*, 2018, **81**, 1690-1704.
10. H. Sun, Z. Yan, F. Liu, W. Xu, F. Cheng and J. Chen, *Adv. Mater.*, 2019, **0**, 1806326.
11. A. W. Jensen, G. W. Sievers, K. D. Jensen, J. Quinson, J. A. Arminio-Ravelo, V. Brüser, M. Arenz and M. Escudero-Escribano, *J. Mater. Chem. A*, 2020, **8**, 1066-1071.
12. G. Dong, M. Fang, J. Zhang, R. Wei, L. Shu, X. Liang, S. Yip, F. Wang, L. Guan, Z. Zheng and J. C. Ho, *J. Mater. Chem. A*, 2017, **5**, 11009-11015.
13. R. N. Singh, D. Mishra, Anindita, A. S. K. Sinha and A. Singh, *Electrochem. Commun.*, 2007, **9**, 1369-1373.
14. A. Li, H. Ooka, N. Bonnet, T. Hayashi, Y. Sun, Q. Jiang, C. Li, H. Han and R. Nakamura, *Angew. Chem. Int. Ed.*, 2019, **58**, 5054-5058.
15. P. Jiang, Q. Liu, Y. Liang, J. Tian, A. M. Asiri and X. Sun, *Angew. Chem. Int. Ed.*, 2014, **53**, 12855-12859.
16. B. Liu, Y.-F. Zhao, H.-Q. Peng, Z.-Y. Zhang, C.-K. Sit, M.-F. Yuen, T.-R. Zhang, C.-S. Lee and W.-J. Zhang, *Adv. Mater.*, 2017, **29**, 1606521.
17. Y. Pi, Q. Shao, P. Wang, F. Lv, S. Guo, J. Guo and X. Huang, *Angew. Chem. Int. Ed.*, 2017, **56**, 4502-4506.
18. Z. Yan, H. Sun, X. Chen, H. Liu, Y. Zhao, H. Li, W. Xie, F. Cheng and J. Chen, *Nat. Comm.*, 2018, **9**, 2373.
19. Y.-P. Zhu, Y.-P. Liu, T.-Z. Ren and Z.-Y. Yuan, *Adv. Funct. Mater.*, 2015, **25**, 7337-7347.
20. Y. Wang, G. Zhang, W. Xu, P. Wan, Z. Lu, Y. Li and X. Sun, *ChemElectroChem*, 2014, **1**, 1138-1144.
21. Y. Liu, X. Liang, L. Gu, Y. Zhang, G.-D. Li, X. Zou and J.-S. Chen, *Nat. Comm.*, 2018, **9**, 2609.
22. K. Xu, F. Wang, Z. Wang, X. Zhan, Q. Wang, Z. Cheng, M. Safdar and J. He, *ACS Nano*, 2014, **8**, 8468-8476.

23. X. Zhang, Y. Zhang, B.-B. Yu, X.-L. Yin, W.-J. Jiang, Y. Jiang, J.-S. Hu and L.-J. Wan, *J. Mater. Chem. A*, 2015, **3**, 19277-19281.
24. C. Roy, B. Sebok, S. B. Scott, E. M. Fiordaliso, J. E. Sørensen, A. Bodin, D. B. Trimarco, C. D. Damsgaard, P. C. K. Vesborg, O. Hansen, I. E. L. Stephens, J. Kibsgaard and I. Chorkendorff, *Nat. Catal.*, 2018, **1**, 820-829.
25. T. Kou, S. Wang, J. L. Hauser, M. Chen, S. R. J. Oliver, Y. Ye, J. Guo and Y. Li, *ACS Energy Lett.*, 2019, **4**, 622-628.
26. F. Song, M. M. Busch, B. Lassalle-Kaiser, C.-S. Hsu, E. Petkucheva, M. Bensimon, H. M. Chen, C. Corminboeuf and X. Hu, *ACS Cent. Sci.*, 2019, **5**, 558-568.
27. H. Zhou, F. Yu, J. Sun, R. He, S. Chen, C.-W. Chu and Z. Ren, *Proc. Natl. Acad. Sci. U. S. A.*, 2017, **114**, 5607.
28. F. Yu, H. Zhou, Y. Huang, J. Sun, F. Qin, J. Bao, W. A. Goddard, S. Chen and Z. Ren, *Nat. Comm.*, 2018, **9**, 2551.
29. P. F. Liu, X. Li, S. Yang, M. Y. Zu, P. Liu, B. Zhang, L. R. Zheng, H. Zhao and H. G. Yang, *ACS Energy Lett.*, 2017, **2**, 2257-2263.
30. P. Bera, *Int. J. Self-Propag. High-Temp Synth.*, 2019, **28**, 77-109.
31. M. G. Chourashiya and A. Urakawa, *J. Mater. Chem. A*, 2017, **5**, 4774-4778.
32. A. Singhal, A. Bisht, A. Kumar and S. Sharma, *J. Electroanal. Chem.*, 2016, **776**, 152-161.
33. T. Pandiarajan, S. Ravichandran and L. J. Berchmans, *RSC Advances*, 2014, **4**, 64364-64370.
34. E. A. Cochran, K. N. Woods, D. W. Johnson, C. J. Page and S. W. Boettcher, *J. Mater. Chem. A*, 2019, **7**, 24124-24149.
35. K. Rajeshwar and N. R. de Tacconi, *Chem. Soc. Rev.*, 2009, **38**, 1984-1998.
36. F. Deganello and A. K. Tyagi, *Prog. Cryst. Growth Charact. Mater.*, 2018, **64**, 23-61.
37. F.-t. Li, J. Ran, M. Jaroniec and S. Z. Qiao, *Nanoscale*, 2015, **7**, 17590-17610.
38. A. Varma, A. S. Mukasyan, A. S. Rogachev and K. V. Manukyan, *Chem. Rev.*, 2016, **116**, 14493-14586.
39. M.-G. Kim, M. G. Kanatzidis, A. Facchetti and T. J. Marks, *Nat. Mater.*, 2011, **10**, 382-388.
40. H. Wang, H.-W. Lee, Y. Deng, Z. Lu, P.-C. Hsu, Y. Liu, D. Lin and Y. Cui, *Nat. Comm.*, 2015, **6**, 7261.
41. X. Long, Z. Ma, H. Yu, X. Gao, X. Pan, X. Chen, S. Yang and Z. Yi, *J. Mater. Chem. A*, 2016, **4**, 14939-14943.
42. Q. Kong, W. Feng, Q. Zhang, P. Zhang, Y. Sun, Y. Yin, Q. Wang and C. Sun, *ChemCatChem*, 2019, **11**, 3004-3009.
43. P. A. Sheena, H. Hitha, A. Sreedevi and T. Varghese, *J. Mater. Sci.: Mater. Electron.*, 2020, **31**, 5769-5778.
44. A. Stokłosa, *Ionics*, 2011, **17**, 271-285.
45. I. J. Pickering, G. N. George, J. T. Lewandowski and A. J. Jacobson, *J. Am. Chem. Soc.*, 1993, **115**, 4137-4144.
46. G. Fu, X. Wen, S. Xi, Z. Chen, W. Li, J.-Y. Zhang, A. Tadich, R. Wu, D.-C. Qi, Y. Du, J. Cheng and K. H. L. Zhang, *Chem. Mater.*, 2019, **31**, 419-428.
47. A. Anspoks, A. Kuzmin, A. Kalinko and J. Timoshenko, *Solid State Commun.*, 2010, **150**, 2270-2274.
48. G. J. Colpas, M. J. Maroney, C. Bagyinka, M. Kumar, W. S. Willis, S. L. Suib, P. K. Mascharak and N. Baidya, *Inorg. Chem.*, 1991, **30**, 920-928.
49. .

50. A. Kuzmin and J. Chaboy, *IUCrJ*, 2014, **1**, 571-589.
51. G. Agostini, A. Piovano, L. Bertinetti, R. Pellegrini, G. Leofanti, E. Groppo and C. Lamberti, *J. Phys. Chem. C*, 2014, **118**, 4085-4094.
52. P. Schrapers, S. Mebs, S. Goetzl, S. E. Hennig, H. Dau, H. Dobbek and M. Haumann, *PLOS ONE*, 2016, **11**, e0158681.
53. T. E. Westre, P. Kennepohl, J. G. DeWitt, B. Hedman, K. O. Hodgson and E. I. Solomon, *J. Am. Chem. Soc.*, 1997, **119**, 6297-6314.
54. K.-W. Nam, M. G. Kim and K.-B. Kim, *J. Phys. Chem. C*, 2007, **111**, 749-758.
55. J. A. Rees, V. Martin-Diaconescu, J. A. Kovacs and S. DeBeer, *Inorg. Chem.*, 2015, **54**, 6410-6422.
56. T. Y. Ma, S. Dai, M. Jaroniec and S. Z. Qiao, *J. Am. Chem. Soc.*, 2014, **136**, 13925-13931.
57. M.-R. Gao, X. Cao, Q. Gao, Y.-F. Xu, Y.-R. Zheng, J. Jiang and S.-H. Yu, *ACS Nano*, 2014, **8**, 3970-3978.
58. Y. Liu, H. Cheng, M. Lyu, S. Fan, Q. Liu, W. Zhang, Y. Zhi, C. Wang, C. Xiao, S. Wei, B. Ye and Y. Xie, *J. Am. Chem. Soc.*, 2014, **136**, 15670-15675.
59. S. Yagi, I. Yamada, H. Tsukasaki, A. Seno, M. Murakami, H. Fujii, H. Chen, N. Umezawa, H. Abe, N. Nishiyama and S. Mori, *Nat. Comm.*, 2015, **6**, 8249.
60. M. Gong, Y. Li, H. Wang, Y. Liang, J. Z. Wu, J. Zhou, J. Wang, T. Regier, F. Wei and H. Dai, *J. Am. Chem. Soc.*, 2013, **135**, 8452-8455.
61. Z. Zhao, H. Wu, H. He, X. Xu and Y. Jin, *Adv. Funct. Mater.*, 2014, **24**, 4698-4705.
62. D. Friebel, M. W. Louie, M. Bajdich, K. E. Sanwald, Y. Cai, A. M. Wise, M.-J. Cheng, D. Sokaras, T.-C. Weng, R. Alonso-Mori, R. C. Davis, J. R. Bargar, J. K. Nørskov, A. Nilsson and A. T. Bell, *J. Am. Chem. Soc.*, 2015, **137**, 1305-1313.
63. C. Tang, H.-F. Wang, H.-S. Wang, F. Wei and Q. Zhang, *J. Mater. Chem. A*, 2016, **4**, 3210-3216.
64. M. S. Burke, M. G. Kast, L. Trotochaud, A. M. Smith and S. W. Boettcher, *J. Am. Chem. Soc.*, 2015, **137**, 3638-3648.
65. D. C. Joshi, S. Nayak, A. Kumar, A. Mohanta, D. Pamu and S. Thota, *J. Appl. Phys.*, 2016, **119**, 074303.
66. W. D. Chemelewski, H.-C. Lee, J.-F. Lin, A. J. Bard and C. B. Mullins, *J. Am. Chem. Soc.*, 2014, **136**, 2843-2850.
67. M. Cui, X. Ding, X. Huang, Z. Shen, T.-L. Lee, F. E. Oropeza, J. P. Hofmann, E. J. M. Hensen and K. H. L. Zhang, *Chem. Mater.*, 2019, **31**, 7618-7625.
68. J. Li, D. Chu, H. Dong, D. R. Baker and R. Jiang, *J. Am. Chem. Soc.*, 2020, **142**, 50-54.
69. S. Watzele, P. Hauenstein, Y. Liang, S. Xue, J. Fichtner, B. Garlyyev, D. Scieszka, F. Claudel, F. Maillard and A. S. Bandarenka, *ACS Catal.*, 2019, **9**, 9222-9230.
70. L. Negahdar, F. Zeng, S. Palkovits, C. Broicher and R. Palkovits, *ChemElectroChem*, 2019, **6**, 5588-5595.
71. T. Zhang, M. R. Nellist, L. J. Enman, J. Xiang and S. W. Boettcher, *ChemSusChem*, 2019, **12**, 2015-2021.
72. M. B. Stevens, L. J. Enman, A. S. Batchellor, M. R. Cosby, A. E. Vise, C. D. M. Trang and S. W. Boettcher, *Chem. Mater.*, 2017, **29**, 120-140.
73. J. Yan, L. Kong, Y. Ji, J. White, Y. Li, J. Zhang, P. An, S. Liu, S.-T. Lee and T. Ma, *Nat. Comm.*, 2019, **10**, 2149.
74. S. Corby, M.-G. Tecedor, S. Tengeler, C. Steinert, B. Moss, C. A. Mesa, H. F. Heiba, A. A. Wilson, B. Kaiser, W. Jaegermann, L. Francàs, S. Gimenez and J. R. Durrant, *Sustain. Energy Fuels*, 2020, **4**, 5024-5030.

75. K. He, T. Tadesse Tsega, X. Liu, J. Zai, X.-H. Li, X. Liu, W. Li, N. Ali and X. Qian, *Angew. Chem. Int. Ed.*, 2019, **58**, 11903-11909.
76. O. Kohmoto, H. Nakagawa, Y. Isagawa and A. Chayahara, *J. Magn. Magn. Mater.*, 2001, **226-230**, 1629-1630.
77. H. Sato, T. Minami, S. Takata and T. Yamada, *Thin Solid Films*, 1993, **236**, 27-31.
78. J. Yu, K. M. Rosso and S. M. Bruemmer, *J. Phys. Chem. C*, 2012, **116**, 1948-1954.
79. B. Bera, A. Chakraborty, T. Kar, P. Leuaa and M. Neergat, *J. Phys. Chem. C*, 2017, **121**, 20850-20856.
80. H. B. Yang, J. Miao, S.-F. Hung, J. Chen, H. B. Tao, X. Wang, L. Zhang, R. Chen, J. Gao, H. M. Chen, L. Dai and B. Liu, *Sci. Adv.*, 2016, **2**, e1501122.
81. L. Francàs, S. Corby, S. Selim, D. Lee, C. A. Mesa, R. Godin, E. Pastor, I. E. L. Stephens, K.-S. Choi and J. R. Durrant, *Nat. Comm.*, 2019, **10**, 5208.
82. K. V. Rao and A. Smakula, *J. Appl. Phys.*, 1965, **36**, 2031-2038.